HAL open science

The transition to aeration in turbulent two-phase mixing in stirred vessels

Lyes Kahouadji, Fuyue Liang, Juan P. Valdes, Seungwon Shin, Jalel Chergui, Damir Juric, Richard V. Craster, Omar K. Matar

To cite this version:

Lyes Kahouadji, Fuyue Liang, Juan P. Valdes, Seungwon Shin, Jalel Chergui, et al.. The transition to aeration in turbulent two-phase mixing in stirred vessels. FLOW, 2022, 2, pp.E30. 10.1017/flo.2022.24 . hal-02994847v1

HAL Id: hal-02994847

https://hal.science/hal-02994847v1

Submitted on 13 Sep 2022 (v1), last revised 8 Nov 2020 (v2)

HAL is a multi-disciplinary open access archive for the deposit and dissemination of scientific research documents, whether they are published or not. The documents may come from teaching and research institutions in France or abroad, or from public or private research centers.

L'archive ouverte pluridisciplinaire **HAL**, est destinée au dépôt et à la diffusion de documents scientifiques de niveau recherche, publiés ou non, émanant des établissements d'enseignement et de recherche français ou étrangers, des laboratoires publics ou privés.

Flow (2022), **x**:0 1–18
doi:xxx

FLOW CAMBRIDGE UNIVERSITY PRESS

RESEARCH ARTICLE

The transition to aeration in turbulent two-phase mixing in stirred vessels

Lyes Kahouadji[1*], Fuyue Liang[1], Juan P. Valdes[1], Seungwon Shin[2], Jalel Chergui[3], Damir Juric[3,4], Richard V. Craster[5] and Omar K. Matar[1].

[1]Department of Chemical Engineering, Imperial College London, South Kensington Campus, London SW7 2AZ, United Kingdom
[2]Department of Mechanical and System Design Engineering, Hongik University, Seoul 04066, Republic of Korea
[3]Université Paris Saclay, Centre National de la Recherche Scientifique (CNRS), Laboratoire Interdisciplinaire des Sciences du Numérique (LISN), 91400 Orsay, France
[4]Department of Applied Mathematics and Theoretical Physics, University of Cambridge, Centre for Mathematical Sciences, Wilberforce Road, Cambridge CB3 0WA, United Kingdom
[5]Department of Mathematics, Imperial College London, South Kensington Campus, London SW7 2AZ, United Kingdom
*Corresponding author. E-mail: l.kahouadji@imperial.ac.uk

Received: XX 2022; **Revised:** XX XX 2022; **Accepted:** XX XX 2022

Fundamental Keywords: Stirred vessels; Multiphase mixing; Turbulence; Aeration;

Application Keywords: Fast-moving consumer goods;

Abstract

We consider the mixing of a viscous fluid by the rotation of a pitched blade turbine inside an open, cylindrical tank, with air as the lighter fluid above. To examine the flow and interfacial dynamics, we utilise a highly-parallelised implementation of a hybrid front-tracking/level-set method that employs a domain-decomposition parallelisation strategy. Our numerical technique is designed to capture faithfully complex interfacial deformation, and changes of topology, including interface rupture and dispersed phase coalescence. As shown via transient, three-dimensional direct numerical simulations, the impeller induces the formation of primary vortices that arise in many idealised rotating flows as well as several secondary vortical structures resembling Kelvin-Helmholtz, vortex breakdown, blade tip vortices, and end-wall corner vortices. As the rotation rate increases, a transition to 'aeration' is observed when the interface reaches the rotating blades leading to the entrainment of air bubbles into the viscous fluid and the creation of a bubbly, rotating, free surface flow. The mechanisms underlying the aeration transition are probed as are the routes leading to it, which are shown to exhibit a strong dependence on flow history.

Impact Statement

The combination of innovative numerical algorithms in a single numerical framework, able to accurately handle coupled physics in fluid mechanics such as multiphase interface motion, fluid-structure interaction and turbulence modelling, is essential for predicting complex mixing flow in stirred vessels. Moreover, a robust high-performance computing architecture enables in-depth understanding of previously inaccessible physics for such extreme flow regimes. In the context of aeration due to mixing in a stirred vessel, where the density ratio between the air and the liquid is $\sim O(10^3)$, it is crucial to provide an accurate numerical framework able to encompass all the techniques listed above.

© The Author(s), 2021. Published by Cambridge University Press. This is an Open Access article, distributed under the terms of the Creative Commons Attribution licence (http://creativecommons.org/licenses/by/4.0/), which permits unrestricted re-use, distribution, and reproduction in any medium, provided the original work is properly cited.

1. Introduction

Flow mixing inside a stirred vessel occurs in a large array of industrial applications and produces complex dynamical structures. These structures, such as those seen in the work of Batels et al. (2002) for single-phase flow, exert a strong influence on the mixing efficiency. Many fast-moving consumer goods involve the manufacturing of so-called structured products (e.g., foods, creams, detergents), which, in turn, result from the multiphase mixing of several types of base products in an open stirred vessel similar to the one shown schematically in Fig. 1. Some viscous products require rapid mixing but in the absence of bubble creation that lead to undesirable partial bottle-filling and process inefficiencies. In contrast, for other processes, such as those used in ice cream manufacturing (involving non-Newtonian fluids and emulsifiers (McClements, 2004; Douglas Goff, 1997)) and those that deploy bioreactors, the promotion of 'aeration' is essential. Thus it is crucial to predict the mixing patterns in stirred vessels, and to demarcate the aeration threshold as a function of the relevant system parameters, such as fluid properties, and impeller geometry and rotational speed.

Given the broad range of applications, there have been numerous studies within the fluid mechanics mixing community which have focused on flow sandwiched between a rotating disk at the base of a cylinder and a free surface. These studies have covered steady and unsteady, axisymmetric and three-dimensional, and flat as well as deoformable free surface flows. The visualisations of Spohn (1991) demonstrated development of an intriguing variety of secondary toroidal structures, which form even under steady, laminar, and axisymmetric conditions. Spohn (1991) and Spohn et al. (1993, 1998) reported that the secondary circulation was not always located along the rotating axis, as for an enclosed cavity but could also be attached to the interface. Daube (1991) performed the first axisymmetric direct numerical simulation assuming a flat, stress-free, free surface, which was later extended by Lopez (1995).

The deformation of the free surface created by the rotating disk was explored experimentally by Vatistas (1990). The interface shape initially forms an inverted bell, and as the rotation rate increases, the free surface descends to the rotating disk producing a dry region on the disk in the form of a periodic pattern in the azimuthal direction. Experiments for flows creating sloshing (Vatistas et al., 1992) have provided a flow pattern map that highlights the most unstable azimuthal modes as a function of the fluid height at rest as a function of the disk angular velocity. The experimental work of Suzuki et al. (2006) and Jansson et al. (2006) studied the variation of the height of the free surface at the axis of symmetry as a function of the Reynolds number (defined using the disk rotational speed and diameter). Four states are described by increasing the Reynolds number: an axisymmetric and steady-state where the interface resembles an inverted bell; a switching state where the interface reaches the rotating disk and dries it from its centre; an asymmetric state with the interface assuming the shape of two rotating concave surfaces; and a state in which the interface regains its symmetrical shape forming a single axisymmetric concavity. Jansson et al. (2006) provided a flow regime map that highlights the unstable azimuthal mode as a function of the disk speed and the flow aspect ratio (fluid height/tank radius). Piva & Meiburg (2005) proposed a first numerical approximation to detect the free surface deflection but this is limited to small deformations. Kahouadji & Martin Witkowski (2014) performed a numerical study that takes into account the axisymmetric interfacial deformation using curvilinear coordinates.

In all of the work reviewed in the forgoing, the motion is driven by a rotating disk rather than an impeller with far fewer studies focusing on the detailed fluid dynamics associated with the latter. With the added complexity of a bladed impeller, we expect to see flow regimes reminiscent of this complex behaviour. Ciofalo et al. (1996) performed a three-dimensional turbulent flow simulation, where the flow equations are in the rotating reference frame of the impeller with the addition of a conventional linear logarithmic "wall function" as in Launder & Spalding (1974). Brucato et al. (1998) compared alternative computational methods: the first replaced the impeller by suitable boundary conditions, and the second consisted of dividing the computational domain into two concentric and partially-overlapping parts; the inner region, containing the impeller, where the flow is simulated in the impeller rotating reference frame, while in the outer region, simulations are conducted in the laboratory reference frame. This technique requires information exchange between the two regions. More recently, Witz et al. (2016)

used the lattice Boltzmann method to simulate the flow in aerated bioreactors, and Li et al. (2017) coupled a volume-of-fluid method to a Reynolds stress model to capture the gas-liquid interface and turbulent flow agitated by pitched blade turbines where the interface deflection reached the impeller hub.

To the best of our knowledge, studies involving unsteady, turbulent, and high deformable free surface flows have been restricted to situations wherein the interface deflection does not descend beyond the impeller blades. As a result, these studies are unable to analyse, in detail, the rich and complex vortical structures accompanying such flows. Furthermore, the phenomenon of aeration has not yet been studied in detail via numerical simulations despite its obvious importance to industrial applications as highlighted above. Aeration involves the development of sufficiently large interfacial deformations that lead to the interaction of the free surface with the rotating impeller. This, in turn, brings about the entrainment and dispersion of the lighter phase into the underlying denser phase; for gas (air)-liquid systems, the dispersed phase corresponds to bubbles (of air).

Our aim in the present paper is to study the intricacies of two-phase mixing flows in a stirred vessel via a standard LES (Large Eddy Simulation) Smagorinsky-Lilly turbulence model coupled with a Direct-Forcing Method for the motion of the impeller (Fadlun et al., 2000; Mohd-Yusof, 1997). Moreover, our numerical framework is formulated in the context of a high-fidelity front-tracking technique for the interface Shin et al. (2017); Shin et al. (2018) which is able to handle complex interfacial deformation, pinchoff and coalescence. Applying this new numerical scheme for stirred vessels, our results elucidate, for the first time, the challenging transition to aeration and its dependence on flow history (e.g., ramping up impulsively from a stationary state vs. increasing the impeller rotational speed following the achievement of a steady-state at lower speeds). A crucial metric for mixing-induced aeration that a numerical framework should be capable of furnishing is the gas/air holdup which corresponds to the relative amount of gas/air held in the liquid phase. We provide results for the temporal variation of the holdup from our simulation data.

The rest of this article is organised as follows. Section 2 describes the configuration, sets out the governing equations, and summarises the computational methods. Section 4 presents results for both laminar and turbulent regimes highlighting the vortical structures occurring in such flows; the mechanisms leading to aeration are described, followed by a discussion of the turbulent aeration regime. Finally, in Section 5, concluding remarks are provided, and ideas for future work are outlined.

2. Problem formulation

The configuration we consider is shown in Fig. 1 and consists of a cylindrical vessel of diameter $D_b = 8.5$ cm filled with a viscous fluid up to a height $h = 7$ cm. The fluid in all simulations is taken to be water or glycerine with air above. The impeller consists of a cylindrical shaft of 0.5 cm diameter, a cylindrical hub of 1 cm diameter and 0.9 cm height, and four blades of 2.5 cm length, 1 cm height, 0.2 cm width, and inclined at $\alpha = 45°$. The impeller is immersed inside the vessel with clearance $C = 3.5$ cm from the bottom of the vessel, and rotating at frequency f. The impeller diameter is $D_i = 5$ cm giving a ratio of radii between the vessel and the impeller $D_b/D_i = 1.7$. The characteristic length, velocity, and pressure scales are the impeller diameter, D_i, blade tip speed, $\pi f D_i$, and $\rho\,(\pi f D_i)^2$, respectively that determine the Reynolds, Froude, and Weber numbers given by:

$$Re = \frac{\rho_l \pi f {D_i}^2}{\mu_l}, \quad Fr = \frac{\pi^2 f^2 D_i}{g}, \quad We = \frac{\rho_l \pi^2 f^2 {D_i}^3}{\sigma}. \tag{1}$$

We solve the Navier-Stokes equations, assuming incompressible and immiscible viscous fluids in a three-dimensional Cartesian domain $\mathbf{x} = (x, y, z) \in [0, 8.6]^2 \times [0, 13]$ cm:

$$\begin{gathered} \nabla \cdot \bar{\mathbf{u}} = 0, \\ \rho \left(\frac{\partial \bar{\mathbf{u}}}{\partial t} + \bar{\mathbf{u}} \cdot \nabla \bar{\mathbf{u}} \right) = -\nabla \bar{p} + \nabla \cdot \left[\left(\mu + \rho C_s^2 \Delta^2 \left| \bar{S} \right| \right) \left(\nabla \bar{\mathbf{u}} + \nabla \bar{\mathbf{u}}^T \right) \right] + \rho \mathbf{g} + \mathbf{F} + \mathbf{F_{fsi}}. \end{gathered} \tag{2}$$

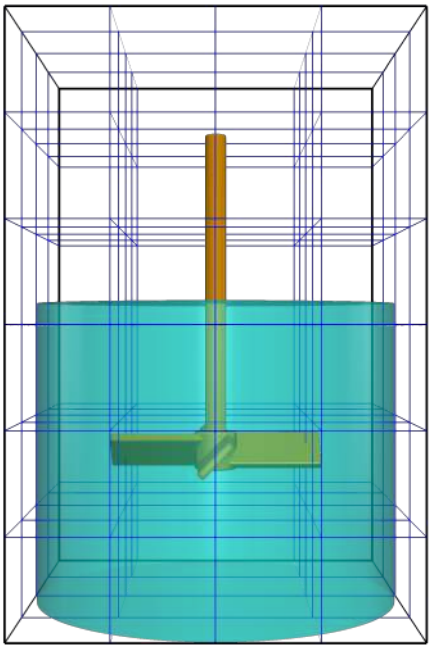

Figure 1. *Schematic illustration of the computational domain: a stirred vessel defined by an open cylindrical container, partially-filled with a viscous liquid, with a pitched-blade turbine immersed within it. The domain is of size* $8.6 \times 8.6 \times 13$ *cm*^{3} *and is divided into* $4 \times 4 \times 6$ *subdomains. The Cartesian structured grid per subdomain is* 64^3*, which gives a global structured mesh grid of* $256 \times 256 \times 384$.

Eqs. 2, include the Smagorinsky-Lilly LES turbulence model (Smagorinsky, 1963) where $\bar{\mathbf{u}}$ is the ensemble-averaged fluid velocity ($\mathbf{u} = \bar{\mathbf{u}} + \mathbf{u}'$, with $\mathbf{u}'$ being the turbulent velocity fluctuation), t the time, $\bar{p}$, the ensemble-averaged pressure, and $\mathbf{g}$ the gravitational acceleration. C_s is the well known Smagorinsky-Lilly coefficient, $\Delta = V^{1/3}$ where V is the volume of a grid cell, $V = \Delta x \Delta y \Delta z$ and $|\bar{S}| = \sqrt{2\bar{S}_{ij}\bar{S}_{ij}}$ with $\bar{S}_{ij}$ being the strain rate tensor

$$\bar{S}_{ij} = \frac{1}{2}\left(\frac{\partial \bar{u}_i}{\partial x_j} + \frac{\partial \bar{u}_j}{\partial x_i}\right) \tag{3}$$

(Pope, 2000, 2004; Meyers & Sagaut, 2006). In our study, C_s is fixed to the value 0.2 as it is quoted in the literature to vary between $0.1 - 0.3$ (Lilly, 1966, 1967; Deardoff, 1970; Mc Millan & Ferziger, 1979; Pope, 2000). If we set $C_s = 0$, Eqs. (2) reduce to the Navier-Stokes equations, without a turbulence model. $\mathbf{F}$, the local surface tension force, and $\mathbf{F_{fsi}}$ is the solid-fluid interaction force. We define $\mathbf{F}$ using a hybrid formulation (Shin et al., 2017; Shin et al., 2018):

$$\mathbf{F} = \kappa_H \nabla \mathcal{H}(\mathbf{x}, t), \tag{4}$$

where $\mathcal{H}$ is an indicator function equal to zero for the gas phase and unity for the liquid phase, respectively. Numerically, this sharp transition is resolved across 3 to 4 grid cells with a steep, but smooth, numerical Heaviside function generated using a vector distance function computed directly from the tracked interface (Shin, 2007; Shin & Juric, 2009). In Eq. (4), κ_H is twice the mean interface curvature field calculated on an Eulerian grid using:

$$\kappa_H = \frac{\mathbf{F}_L \cdot \mathbf{G}}{\mathbf{G} \cdot \mathbf{G}}, \tag{5}$$

in which $\mathbf{F}_L$ and $\mathbf{G}$ are respectively given by:

$$\begin{aligned} \mathbf{F}_L &= \int_{\Gamma(t)} \sigma \kappa_f \mathbf{n}_f \delta_f \left(\mathbf{x} - \mathbf{x}_f\right) \mathrm{d}s \\ \mathbf{G} &= \int_{\Gamma(t)} \mathbf{n}_f \delta_f \left(\mathbf{x} - \mathbf{x}_f\right) \mathrm{d}s. \end{aligned} \tag{6}$$

In these formulae, σ is the surface tension, assumed constant, $\mathbf{x}_f$ is a parameterisation of the interface, $\Gamma(t)$, and $\delta_f(\mathbf{x}-\mathbf{x}_f)$ is a Dirac distribution that is non-zero only when $\mathbf{x} = \mathbf{x}_f$, $\mathbf{n}_f$ is the unit normal vector to the interface, and $\mathrm{d}s$ is the length of the interface element; κ_f is twice the mean interface curvature obtained from the Lagrangian interface structure. The geometric information corresponding to the unit normal, $\mathbf{n}_f$, and length of the interface element, $\mathrm{d}s$, in $\mathbf{G}$ are computed directly from the Lagrangian interface and then distributed onto an Eulerian grid using the discrete delta function. The details follow Peskin (1977) well-known immersed boundary approach using our procedure for calculating the force and constructing the function field $\mathbf{G}$.

The Lagrangian interface is advected by integrating

$$\frac{\mathrm{d}\mathbf{x}_f}{\mathrm{dt}} = \mathbf{V}, \tag{7}$$

with a second-order Runge-Kutta method where the interface velocity, $\mathbf{V}$, is interpolated from the Eulerian velocity. Incorporating the complex geometry of the impeller and its rotation requires the implementation of the so-called Direct Forcing Method (Mohd-Yusof, 1997; Fadlun et al., 2000), which is done by incorporating a fluid-solid interaction force $\mathbf{F_{fsi}}$ in Eq. (2). This force is defined numerically using the latest step of the temporal integration of (2),

$$\rho \frac{\bar{\mathbf{u}}^{n+1} - \bar{\mathbf{u}}^n}{\Delta t} = \mathrm{local}^n + \mathbf{F}^n_{\mathbf{fsi}}, \tag{8}$$

where "local" stands for the right-hand-side terms of Eq. (2) that contain the convective, pressure gradient, viscous, turbulent, gravitational, and surface tension force terms. Here, the superscripts denote the discrete temporal step in the computation. In the solid part of the domain corresponding to the impeller, $\mathbf{F}^n_{\mathbf{fsi}}$ the forced rotational motion $\mathbf{V}^{n+1}$ is enforced:

$$\bar{\mathbf{u}}^{n+1} = \mathbf{V}^{n+1} = 2\pi f \left((y - y_0), -(x - x_0) \right), \tag{9}$$

where $(x_0, y_0) = (4.3, 4, 3)$ cm are the position of the impeller axis. Hence $\mathbf{F_{fsi}}$ is

$$\mathbf{F}^n_{\mathbf{fsi}} = \rho \frac{\mathbf{V}^{n+1} - \bar{\mathbf{u}}^n}{\Delta t} - \mathrm{local}^n. \tag{10}$$

The no-slip condition is applied for the velocity and the interface on the surface of the impeller parts except for the shaft where we impose a solid rotating motion and axial free-slip condition $\partial \mathbf{u}/\partial z = 0$, otherwise, the interface will remain attached to the shaft.

The computational domain (see Fig. 1) is a rectangular parallelepiped where the entire domain is discretized by a uniform fixed three-dimensional finite-difference mesh and has a standard staggered MAC cell arrangement (Harlow & Welch, 1965). The velocity components $\bar{u}$, $\bar{v}$, and $\bar{w}$ are defined on the corresponding cell faces while the scalar variables (pressure $\bar{p}$, and the distance function ψ) are located at the cell centers. All spatial derivatives are approximated by second-order centred differences. The velocity field is solved by a parallel generalized minimal residual (GMRES) method (Saad, 2003) and the pressure field by a modified parallel 3D multigrid solver (Kwak & Lee, 2004; Shin et al., 2017). Parallelisation is achieved using an algebraic domain decomposition where communication across processes is handled by Message Passing Interface (MPI) protocols.

The chosen pitched-blade turbine shown in Fig. 1 and described in the beginning of this section is built using a combination of primitive geometric objects (planes, cylinders, and rectangular blocks) where each object is defined by a static distance function $\psi(x, y, z)$, positive in the fluid and negative in the solid. The resulting shape in Fig. 1-(c) corresponds to the iso-value $\psi(x, y, z) = 0$. Details on how to construct similar complex objects are described in Kahouadji et al. (2018).

For Eqs. (2), (8), and (10), we use the single-field formulation for the density ρ and viscosity μ:

$$\begin{aligned} \rho(\mathbf{x}, t) &= \rho_g + \left(\rho_l - \rho_g\right) \mathcal{H}(\mathbf{x}, t), \\ \mu(\mathbf{x}, t) &= \mu_g + \left(\mu_l - \mu_g\right) \mathcal{H}(\mathbf{x}, t), \end{aligned} \tag{11}$$

where the subscripts g and l designate the gas and liquid phases, respectively. The indicator function, $\mathcal{H}$, is a Heaviside function, zero in the gas phase and unity in the liquid phase; Numerically $\mathcal{H}$ is resolved with a smooth transition across 3 to 4 grid cells and is generated using a vector distance function $\varphi(\mathbf{x})$, positive for the liquid phase and negative for the gas phase, and is computed directly from the tracked interface (Shin & Juric, 2009). The gas phase is considered as air, with constant physical properties at 20 °C ($\rho_g = 1.205$ kg/m^3 and $\mu_g = 1.825 \times 10^{-5}$ Pa.s). The liquid phase corresponds to either water or glycerine with the following properties: $\rho_l = 1000$ kg/m^3, $\mu_l = 10^{-3}$ Pa.s, and $\sigma = 0.0725$ N/m or $\rho_l = 1261.08$ kg/m^3 and $\mu_l = 1.4$ Pa.s, and $\sigma = 0.064$ N/m, for water and glycerine, respectively. Simulations with glycerine and water allow us to compare the two-phase mixing phenomena associated with laminar and turbulent flow regimes, respectively.

3. Validations

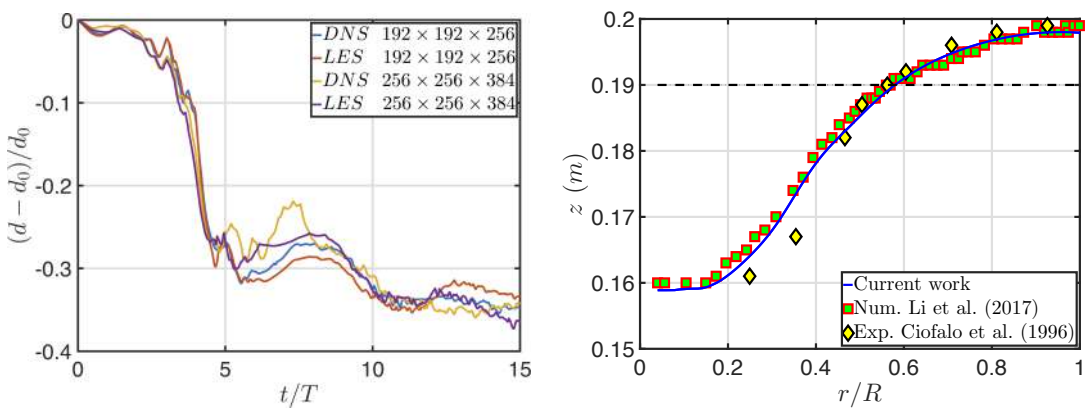

(a) (b)

Figure 2. *Validation of our numerical framework, (a): mesh dependence for the predictions of the interface minimal vertical position normalised by the position at the axis $r = 0$ generated via the DNS and LES approaches with the following parameters $f = 1/T = 8$ Hz, $Re \sim 6.28 \times 10^4$, $Fr \sim 3.22$, and $We \sim 1.1 \times 10^3$, using water properties; (b): comparison with a benchmark case for a developed interface shape Ciofalo et al. (1996) and Li et al. (2017).*

In the previous section, we have detailed the governing equations and the numerical scheme that accounts for fluid-structure interaction applied to a turbulent multiphase mixing vessel. Before moving to the results section, it is crucial to validate this new numerical framework that combines both a direct forcing method for the impeller motion and the hybrid front-tracking/level-set method for tracking the interface in the context of a turbulent two-phase flow in an agitated vessel. Figure 2a, provides evidence of mesh-independence of our numerical solutions by showing the normalised minimum position of the

interface which is often located at the axis $r = 0$ generated via the LES and DNS (Direct Numerical Simulation) approaches. Global meshes of $192 \times 192 \times 256$ and $256 \times 256 \times 384$ are used and results are presented for water agitated at a constant frequency $f = 1/T = 8$ Hz ($Re \sim 6.28 \times 10^4$, $Fr \sim 3.22$, and $We \sim 1.1 \times 10^3$). It is clear from figure 2a that both resolutions lead to accurate predictions of the interface deflection for both DNS and LES approaches. It is also well known through the previous works of Piva & Meiburg (2005) and Kahouadji (2011) that the physical quantity that plays a major role in interface deflection is the azimuthal velocity distribution along the interface, $u_\theta \sim r$ close to the shaft. Therefore, even for turbulent regimes, the interface can be accurately captured via DNS or LES approaches. Thus, the resolution used in the rest of this paper is globally $256 \times 256 \times 384$ with a constant LES model unless specified otherwise.

We also provide further validation involving a direct comparison with previous works of Ciofalo et al. (1996) and Li et al. (2017). The configuration here consists of a cylindrical tank with diameter 0.19m and height of 0.30m filled with a liquid of initial height of 0.19 m and agitated by a pitched blade turbine at 194 r/min ($f \sim 3.23$ Hz) located at a distance ~ 6.3 cm from the bottom. More details of this configuration can be found in Ciofalo et al. (1996) and Li et al. (2017). The physical properties of the liquid working medium is water ($\rho_l = 998$ kg/m^3, $\mu_l = 0.00103$ Pa.s) and the surface tension coefficient between the phases (air and water) is set as 0.0732 N/m. As depicted in figure 2b, our numerical framework is capable of reproducing accurately different stirring configurations. Note that our computation is purely three-dimensional and the resulting interface is axisymmetric.

The examples shown in figure 2 inspire confidence in our new numerical framework which combines a LES model and a direct forcing method for a FSI (Fluid-Structure Interaction) configuration, within the context of a hybrid front-tracking/level-set method for the advection of the interface. Another novelty, and a significant challenge which this study will address, is to simulate the aeration regime that features a multitude of interfacial singularities such as breakup and coalescence at large density ratios, $\sim 10^3$; this is notoriously troublesome for numerical procedures previously used for the simulation of two-phase flows.

4. Results and discussions

We begin the presentation of our results by describing the flow associated with the case of glycerine (Section 4.1) wherein the interface is slightly deformed. In section 4.2, we replace glycerine by water and highlight the emergence of complex vortical structures and a highly deformed surface; a large range of rotating frequencies, from $f = 5$ Hz to 9.5 Hz, is covered. The mechanisms leading to aeration are studied in Section 4.3 by close examination of the transition boundary between the separated and dispersed flows. Finally, Section 4.4 focuses on the situation wherein air is entrained into the water across a highly deformed interface leading to bubbly mixing.

4.1. Laminar vortex mixing

The typical flow in the laminar regime is summarised in Fig. 3. Here, glycerine is chosen as the liquid phase and the rotation frequency is restricted to $f = 1/T = 8$ Hz so that the flow regime remains laminar, and the free surface deformation small, characterised by the following values of the relevant dimensionless numbers: $Re \sim 56$, $Fr \sim 3.22$, and $We \sim 1.55 \times 10^3$. The free surface deformation is defined as 'small' provided the amplitude of the deflection to the horizontal, divided by the characteristic length scale D_i, does not exceed 10%.

A centrifugal force is generated in the vicinity of the rotating blades causing the glycerine solution to spiral out toward the tank periphery (see Fig. 3-(a)). This spiralling motion reaches the fixed vessel wall inducing the formation of two Stewartson boundary layers (Kahouadji & Martin Witkowski, 2014; Poncet, 2005; Stewartson, 1953) at the top and bottom peripheries. The fluid motion reaches the free surface (bottom of the tank), it then decelerates by a centripetal spiral motion toward the rotating shaft (rotation axis) above (below) the impeller; this is analogous to the behaviour reported previously in the

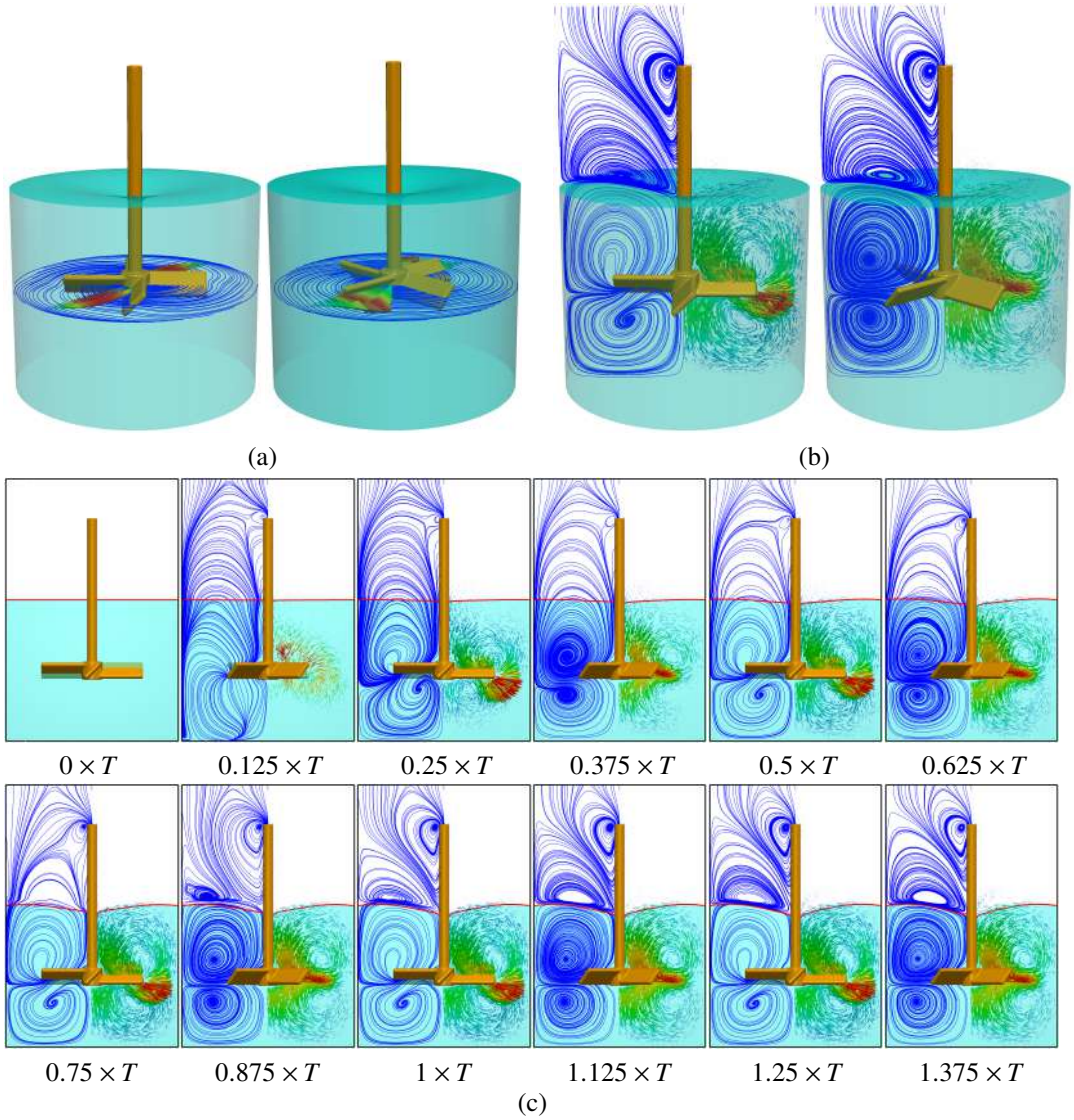

Figure 3. *Laminar mixing flow for the case of glycerine with $f = 1/T = 8\,Hz$ for which the dimensionless numbers are $Re \sim 56$, $Fr \sim 3.22$, and $We \sim 1.55 \times 10^3$. Flow visualisation of the streamlines in the horizontal plane located at $z = 3.95$ cm, (a), and vertical plane $y = 0$, (b); (c) shows snapshots of the streamlines in the $y = 0$ plane that illustrate the temporal evolution of the flow starting from rest. (see Supplementary Material "Animation-Fig3.avi")*

literature for rotating disks (Daube, 1991; Spohn, 1991; Spohn et al., 1993, 1998; Piva & Meiburg, 2005; Kahouadji & Martin Witkowski, 2014). The flow is not axisymmetric, and one can see in Fig. 3-(a) and (b) that the position of the rotating blades matter in terms of understanding the reasons underlying the flow patterns. Under the pumping effect generated by the rotating blades, the fluid returns toward the rotating hub and blades by an upward swirling motion around the z-axis from the bottom, and by a downward swirling motion around the rotating shaft (see Fig. 3-(a) and (b)).

The temporal evolution starting from a static initial condition $t = 0 \times T$ up to $t = 1.375 \times T$ is shown in Fig. 3-(c), which depicts the streamlines in the horizontal plane immediately below the hub as well as in the $y = 0$ plane. From this figure, we can see that the free surface shape becomes essentially steady

for $t > T$. This has similarity with the work of Kahouadji & Martin Witkowski (2014) who studied the free surface rotating flow generated by a rotating disk located at the bottom of a fixed cylindrical tank by solving the steady and axisymmetric Navier-Stokes equations using a vorticity-streamfunction formulation. Assuming a developed steady state, Kahouadji & Martin Witkowski (2014) considered the interface as a streamline. In the present case, as shown in Fig. 3(c), the streamlines cross the interface for $t < T$ indicating interfacial motion, whereas for $t > T$, the interface becomes a streamline and remains steady. It is also noteworthy that although the interfacial shape is steady and axisymmetric for $t > T$, the liquid flow is periodic in its azimuthal direction with a periodicity mode of 4, reflecting the impeller geometry which comprises four blades. Finally, we draw attention to the time required to make the flow quasi-steady: $t \sim T = 1/f = 1/8$ (s); this is in contrast to the cases which will be discussed below where, typically, 10 or $20 \times T$ are required to reach a quasi-steady state.

4.2. Turbulent vortex mixing

We replace the highly viscous glycerine with water and keep the frequency at $f = 8$ Hz so that the flow is characterised by $Re = 6.28 \times 10^4$, $Fr = 3.22$, and $We = 1.08 \times 10^3$, which indicates that it is expected to be turbulent and accompanied by large interfacial deformations. We show in Fig. 4 the spatio-temporal behaviour of the flow for $f = 1/T = 8$ Hz starting from a static initial state until a steady state is reached for $t = 20 \times T$. It is seen that the free surface shape remains quasi-flat until the impeller has rotated 1.5 cycles (see Fig. 4-(a-e)). However, in spite of this, the velocity magnitude on the interface Fig. 4-(d-j) shows that the velocity disturbance experiences a periodic distribution along its azimuthal direction with a wave number equal to 4, a symmetry that once again reflects the impeller 4-blade geometry. At $t = 2 \times T$, the interface starts to deform (see Fig. 4-(f-l)) where the velocity gradient is high, leading to a periodic azimuthal interface deflection with a wave number 4 being preserved. The interface continues to undergo spatio-temporal variations until reaching a quasi-steady and approximately axisymmetric state beyond $t = 10 \times T$, as shown in Fig. 4-(j-l), which is characterised by maximal interfacial deflection.

The evolution of the vortical structures in the vertical plane shows the existence of very rich dynamics, as depicted in Fig. 4. At early times ($t \sim 0.25 \times T$), the impeller blades generate a large primary vortex that starts at the blade tips toward the bottom of the vessel and then moves upward near the vessel wall toward the interface. A secondary vortex is also generated under the impeller blades, which rotates radially in the opposite direction compared to the primary vortex. This secondary vortex is generated from the bottom of the impeller hub and grows until being replaced by a two dipole-vortex, one above and the other below the impeller blades (see the streamlines in Fig. 4-(c) and (d) for $t = 0.5$ and $1 \times T$).

At $t = 1.5 \times T$, the bottom vortex dissipates and we notice the creation of Kelvin-Helmholtz vortices that merge at $t = 2 \times T$ into a single vortex below the impeller blades (see the streamlines in Fig. 4-(e,f)). These Kelvin-Helmholtz vortices are generated due to the fact that the primary top vortex rotates faster (due to the presence of the interface) than the secondary bottom vortex (due to the no-slip condition at the bottom of the vessel), and creates a large shear zone between these two vortices. For $t \geq 2 \times T$, the Kelvin-Helmholtz vortices give way to two large counter-rotating vortices and a small vortex breakdown underneath the impeller hub, a well-known phenomenon in the context of a rotating disk inside a closed cylindrical tank (i.e., a rotor-stator configuration (Daube, 1991; Kahouadji, 2011; Spohn, 1991; Spohn et al., 1998)). These vortical structures described for $f = 8$ Hz are also observed for the entire range of frequency $f \leq 9$ Hz as shown in Fig. 5 which depicts the spatio-temporal evolution of the interface and vortical structures in a two-dimensional plane for $f = 5, 7$, and 9 Hz for $t = 0.25 \times T$-$15 \times T$ (see also the supplementary Material "Animation-Fig5.avi"). Further inspection of Fig. 5 reveals strong qualitative similarities amongst the vortical structures for this range of frequencies (and Re and We) for $t \leq 2 \times T$.

Figure 6-(a)-(f) depicts snapshots of the interface shape, and accompanying structures in the vorticity and pressure fields at $t/T = 20$ for $f = 5 - 9.5$ Hz. It is clear that the salient points highlighted for $f = 8$ Hz in Fig. 4 are observed for the entire frequency range. Figure 6-(g), shows the temporal evolution of the global kinetic energy of the flow, $\kappa = \left(\int\int\int \rho \mathbf{u}^2 dxdydz\right)$, and Fig. 6-(h) shows the variation of

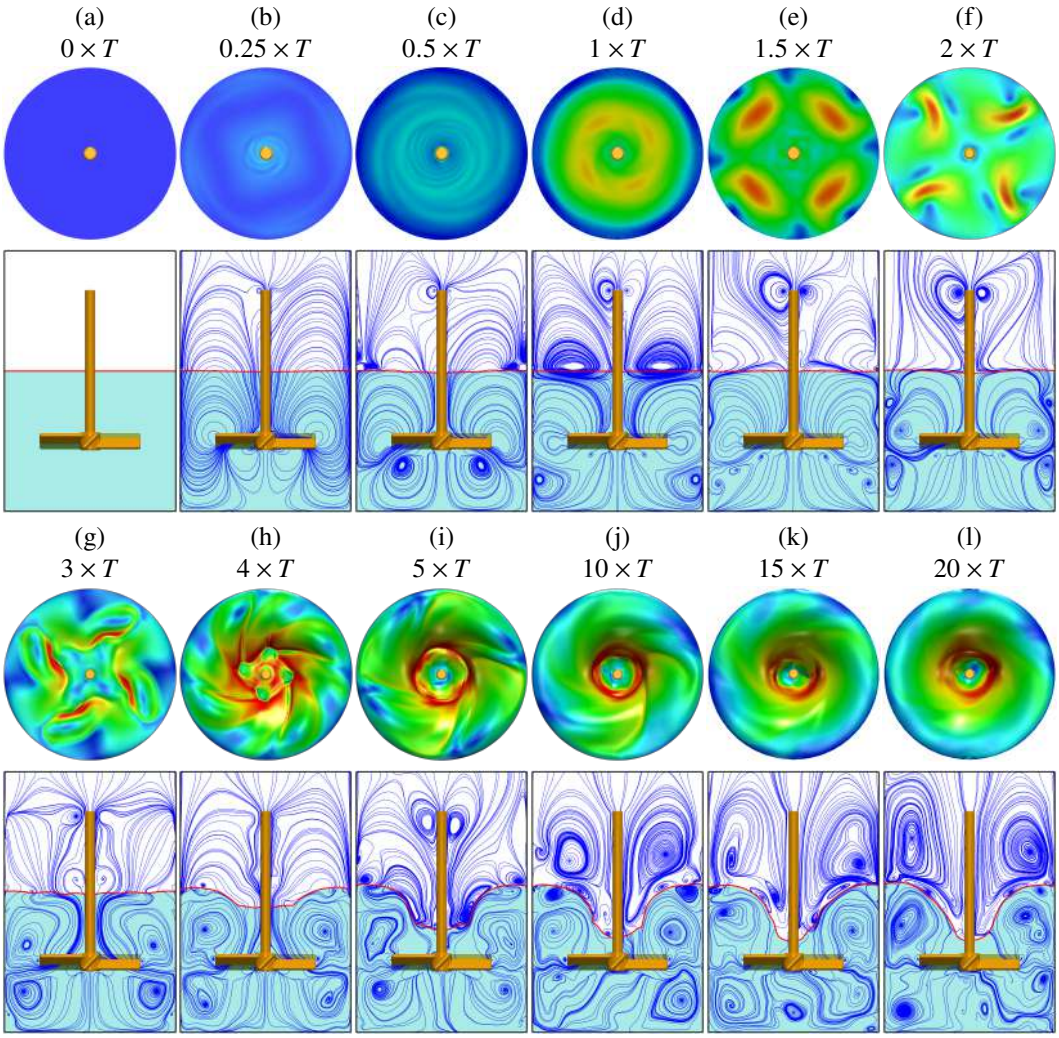

Figure 4. *Spatio-Temporal evolution of the flow for water, vortical structures, and interface shapes coloured by velocity magnitude shown in the lower and upper figures in every panel, respectively, for* $f = 1/T = 8$ *Hz. The dimensionless numbers are* $Re \sim 6.28 \times 10^4$, $Fr \sim 3.22$, $We \sim 1.08 \times 10^3$. *(see Supplementary Material "Animation-Fig4.avi")*

the minimum position of the interface with time for the range of frequency $f = 5$ to 9.5 Hz. For $f = 5$ Hz, the interface deflection is small compared to other cases and a vortex breakdown attached to the interface occurs; this phenomenon is also observed for rotating disks inside an open cavity (Kahouadji & Martin Witkowski, 2014; Piva & Meiburg, 2005; Spohn, 1991; Spohn et al., 1993, 1998). In certain cases, there is an appearance of a small vortex at the bottom corner of the vessel or at the top corner (see Fig. 6-(c) for $f = 7$ Hz). For $f = 9.5$ Hz, the interface just reaches the hub of the impeller (see Fig 6-(f)). For this set of parameters, this frequency represents the limit for efficient mixing without entraining bubbles into the water phase. At $t = 20 \times T$, we consider the flow to be quasi-steady as the curves corresponding to Fig. 6-(g)-(h) flatten, particularly for the range $f = 5 - 8$ Hz. For $f = 9$ and 9.5 Hz, although the kinetic energy appears to plateau for $t \geq 10 \times T$, the minimal interfacial position exhibits small-amplitude, high-frequency oscillations due to the interfacial interactions with the impeller hub.

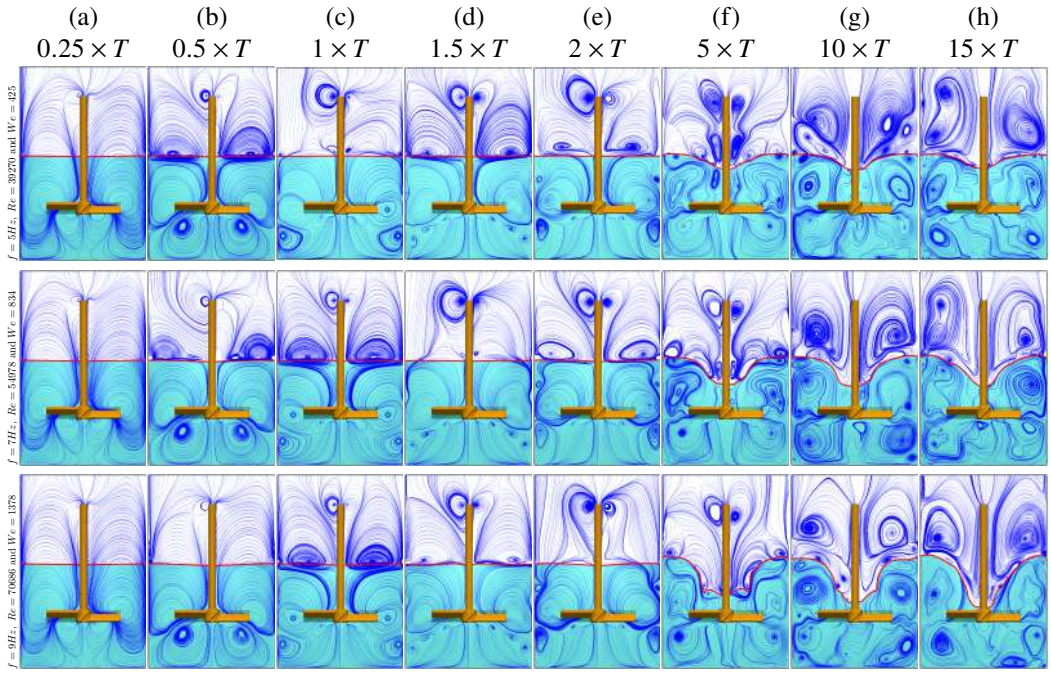

Figure 5. *Spatio-temporal evolution of vortical structures in water for* $f = 1/T = 5$, 7 *and* 9 *Hz, from top to bottom, respectively, and* $t = 0.25 \times T$-$15 \times T$. *The corresponding Reynolds and Weber number combinations are* $(Re, We) = (39270, 425)$, $(54978, 834)$ *and* $(70686, 1378)$, *respectively. (see Supplementary Material "Animation-Fig5.avi")*

The pressure field shown in Fig. 6 for all values of f illustrates the dominance of the vortical structures on the pressure field. For small rotation frequency values ($f \leq 5Hz$), the behaviour of the pressure is hydrostatic, decreasing linearly as a function of z-direction. This type of pressure field distribution is observed for $f = 5$ Hz (see Fig. 6-(a)). Increasing the frequency up to 6 Hz, the pressure field still varies linearly through z-direction; however, a depression zone is noticed at the back of the blades (see pressure field in 6-(b-f)). This depression is a characteristic of flows past an obstacle, which means that in the rotating blades reference, the front and back of the blades are zones of high and low pressure, respectively. In addition to these low and high pressure zones near the blades, we can notice that for high values of rotation frequency ($f \geq 7$ Hz), the eddy structures break the hydrostatic form of the pressure field and a high pressure zone is localised only near the bottom outer edge of the vessel.

4.3. Transition to aeration

In this section, we will focus on the air-water system and elucidate mechanisms that lead to entrainment of air bubbles into the water phase via careful examination of the transition boundary between the vortex and bubbly mixing regimes. In order to perform accurate simulations of the onset of aeration, all simulations presented in this section are performed using $4 \times 4 \times 6 = 96$ subdomains, with a Cartesian structured grid of 64^3 per subdomain, which gives a global structured mesh of $256 \times 256 \times 384$.

Figure 7 depicts the interfacial dynamics associated with the $f = 10$ Hz case, characterised by $Re = 78540$ and $We = 1713$. The results presented thus far were generated by starting from an initially flat interface and a velocity field at rest ($\mathbf{u} = \mathbf{0}$). Using this initialisation it is seen clearly that the interface, which interacts with the impeller hub, undergoes breakup leading to the formation of three small bubbles that are entrained into the water phase. If, however, the simulation is initialised starting

from the steady-state associated with the $f = 8$ Hz case, but with $f = 10$ Hz, then we find that the outcome (not shown) corresponds to a vortex mixing regime, similar to that shown in Fig. 6-(f).

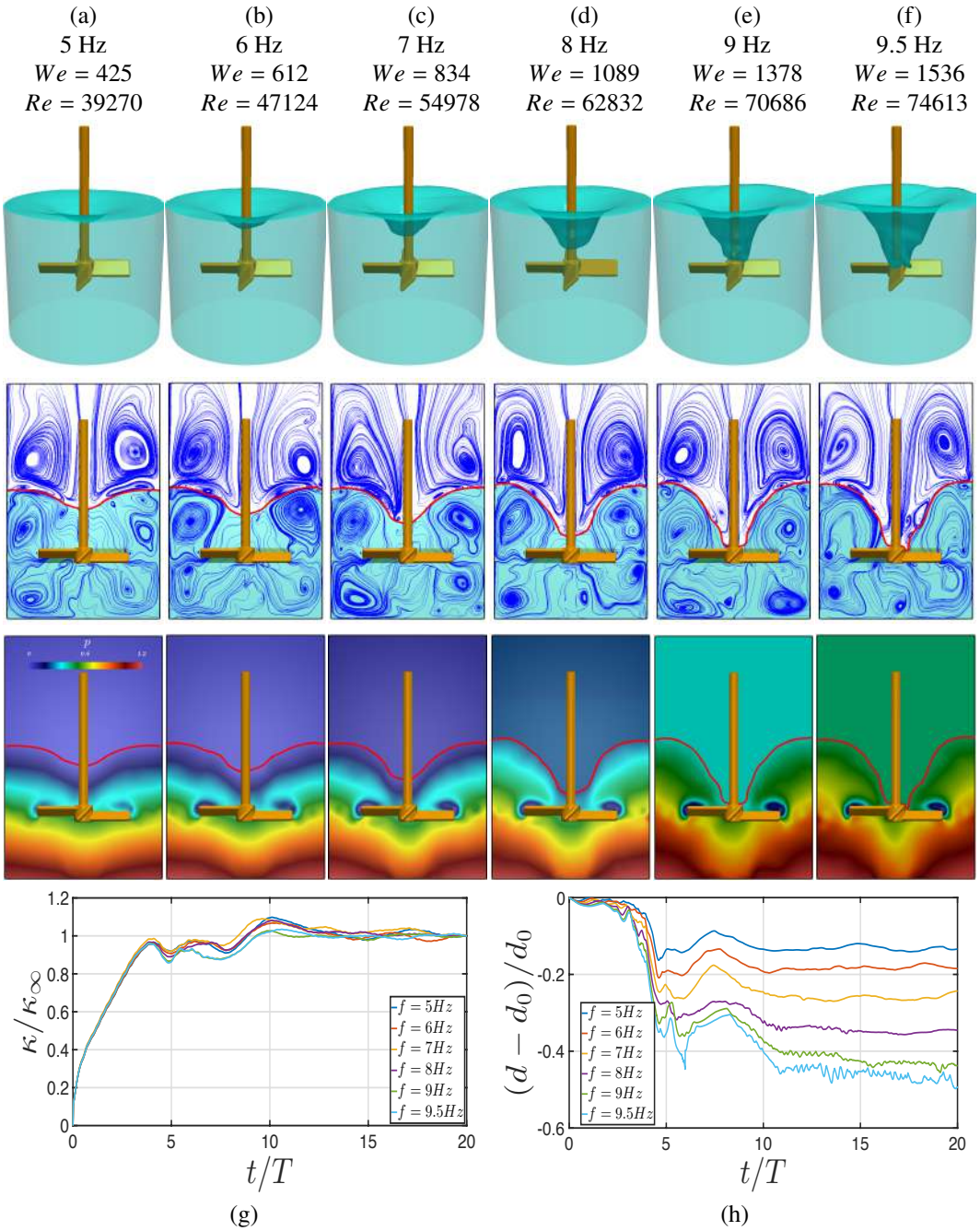

Figure 6. *Interface shape, vortical structures, and pressure fields in a two-dimensional vertical plane at $t/T = 20$ for $f = 5, 6, 7, 8, 9$ and 9.5 Hz, (a)-(f), respectively; (g) and (h) show the temporal evolution of the kinetic energy and minimum interface position normalised by their initial values, respectively. (see Supplementary Material "Animation-Fig6.avi")*

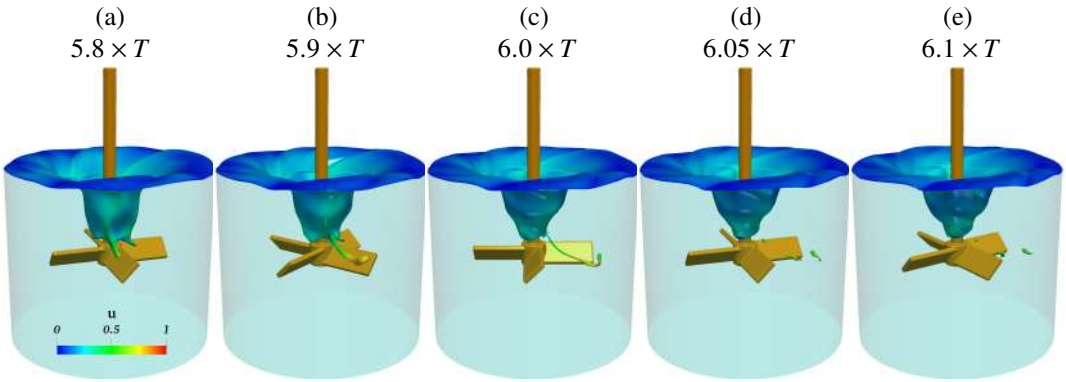

Figure 7. *Spatio-temporal evolution of the mixing behaviour for* $f = 1/T = 10$ *Hz,* $Re = 78540$*, and* $We = 1713$ *highlighting the onset of aeration.*

In order to elucidate the mechanisms underlying aeration, we focus on the case wherein the flow is started impulsively from an initially stationary flat-interface state. As a result of the impeller rotation, a low pressure region forms near the impeller hub that leads to a large interfacial deflection and the formation of a thin air ligament at the back of one of the blades; this is a consequence of the centrifugal forces that drive ligament elongation in the radial direction away from the hub. The ligament eventually undergoes a Rayleigh-Plateau instability and breakups into three small bubbles (see Fig. 7 c, d, and e). Thus, the route to bubble creation, and subsequent aeration of the water phase, involves three successive mechanisms: (i) a sufficiently strong centrifugal force able to deform the interface rapidly toward the impeller hub; (ii) ligament formation that grows radially behind a blade; (iii) a Rayleigh-Plateau-driven breakup of the ligament. The example shown in Fig. 7 features the formation of only one air ligament and its breakup. We will show that further increase in rotating frequency causes simultaneous entrapment and growth of multiple ligaments, leading to a more violent transition to the bubbly mixing regime.

4.4. Bubbly mixing

After the brief discussion of the mechanisms underlying aeration mixing, we now increase the impeller rotation frequency to $f = 11$ Hz ($Re = 86394$ and $We = 2073$) for which the outcome is very bubbly with a total number of air bubbles being of the order of hundreds dispersed inside the water phase. We have performed this calculation using both the DNS & LES approaches and simulations with the former exhibit interesting phenomena such as the bursting effect with the main interface. Figure 8 shows the spatio-temporal evolution of the flow, using DNS where it is seen that the initially flat interface undergoes a rapid deflection (see Fig. 8 a, b, & c) toward the impeller blades (see Fig. 8 e-f) with some interfacial pinchoff without significant ligament formation and breakup (see Fig. 8 g-h).

At $t = 4.25 \times T$, four air ligaments are formed, which grow quickly in the radial direction, and break up into many bubbles (see Fig. 8 i-j). The resulting air-ligaments forming behind each blade are not as thin as in the case described for $f = 10$ Hz (see Fig. 7). As highlighted through Fig. 8 j-k, thick shaped air ligaments will breakup and disperse all around the liquid water phase. This process continues and produces a myriad of multiscale air-bubbles. Some of these bubbles have the shape of elongated thin air ligaments, also dispersed in the water phase, and eventually breakup later into smaller bubbles.

The flow is also accompanied by a series of coalescence events that occur between bubbles inside the water phase as well as with the main top interface. Small bubbles usually remain in the water phase but larger bubbles, due to buoyancy, rise to the top. When any bubble reaches the main top interface, it bursts and sometimes ejects some liquid-droplets above the interface (see Fig. 8 n-o).

In Fig. 9, we have isolated several 'singular' events that involve topological transitions occurring in this type of bubbly mixing. Figure 9a highlights a coalescence event between a small bubble and the main interface. These snapshots in Fig. 9a are given at the following times, from top to bottom, $t/T = 5.92$, 5.94, and 5.96, respectively. We can notice that the small bubble coalesces with the vertical part of the main interface that surrounds the impeller shaft. In Fig. 9b, we have also isolated the breakup event of a ligament. We can notice a rapid coalescence of a tiny bubble with this ligament before experiencing two interfacial breakups later.

Figure 9c shows the temporal evolution of a bubble bursting through the main top interface, generating liquid ligaments above this interface, and finally breaking up into a multitude of droplets that will fall back to the liquid bulk later on. Contrary to the coalescence described in Fig. 9a, when a bubble hits

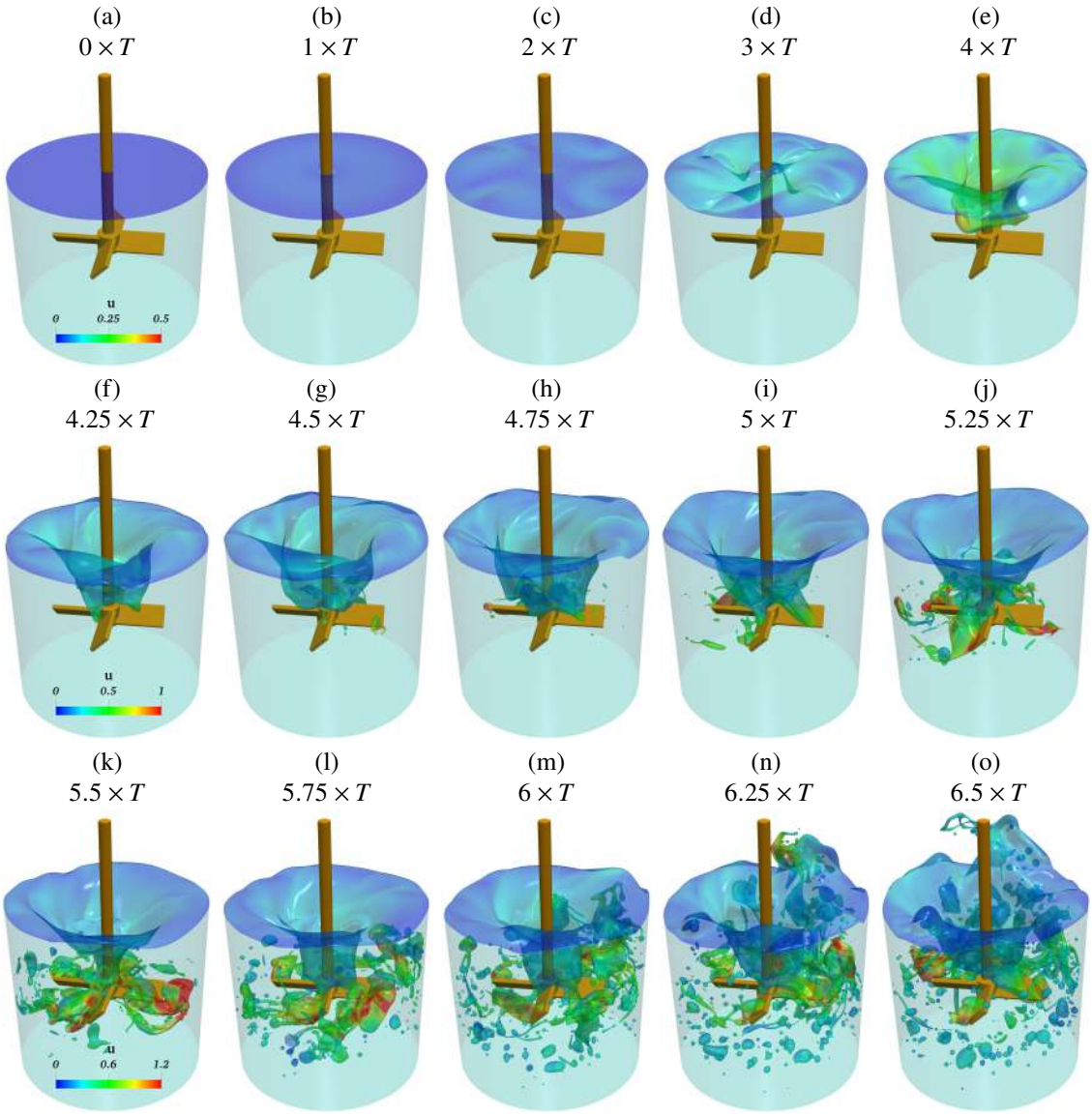

Figure 8. *Spatio-temporal evolution for bubbly mixing with* $f = 1/T = 11$ *Hz,* $Re = 86394$*, and* $We = 2073$.

the top interface, it bursts. However, if a bubble hits the vertical part of the main interface, the outcome corresponds to a simple coalescence process. Furthermore, for the latest snapshot of Fig. 9c, we count a total of 503 bubbles dispersed inside the bulk of the water phase, and also a total 33 water drops. Some of the water drops are located above the main top interface (see the latest snapshots Fig. 9c), but some others are encapsulated within some large bubbles inside the bulk water phase.

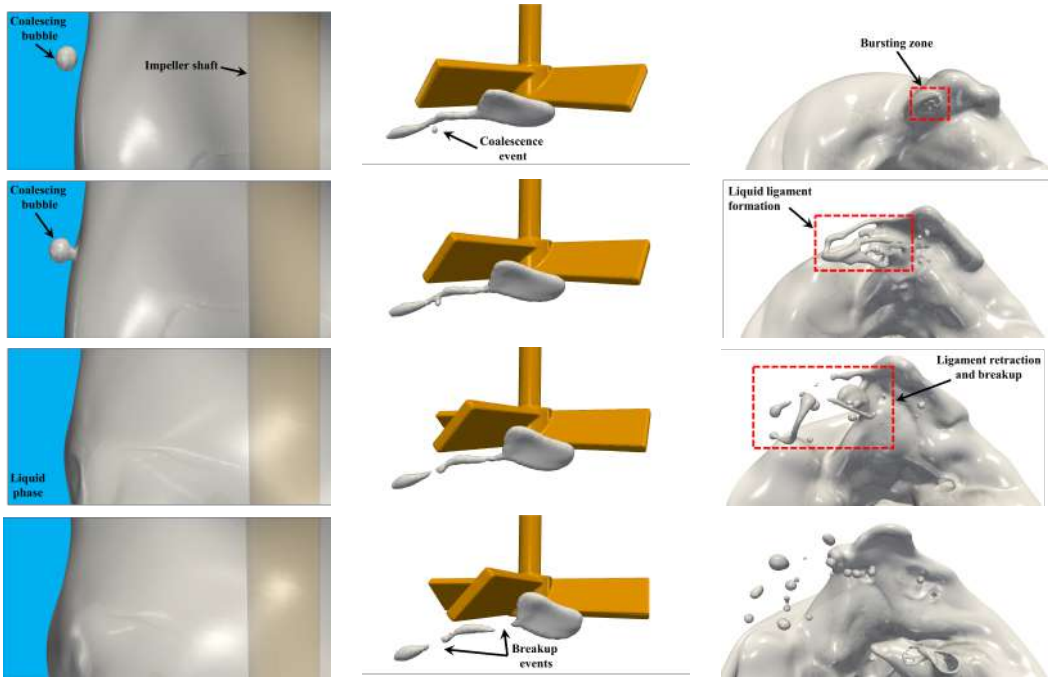

(a) (b) (c)

Figure 9. *Flow snapshots for $f = 1/T = 11$ Hz, $Re = 86394$, and $We = 2073$ showing bubble-interface coalescence, ligament breakup, and bubble bursting through the interface, in (a)-(c), respectively.*

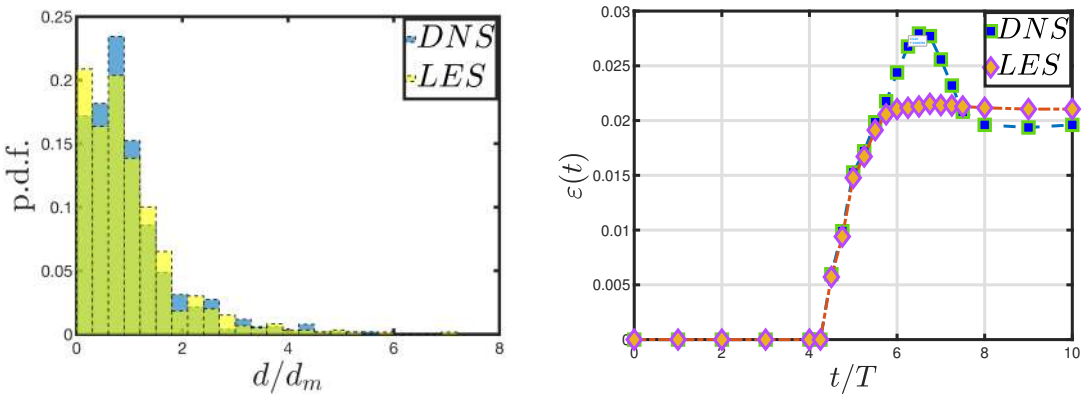

(a) (b)

Figure 10. *Probability density function histogram of bubble size inside the liquid bulk, (a), normalised by the average bubble diameter, d_{bm}, associated with the times $t/T = 10$; temporal evolution of the gas holdup $\varepsilon(t)$ generated using the DNS and LES approaches, (b). The rest of the parameter values are the same as those used to generate Fig. 7.*

At this stage of the mixing process, it is interesting to follow the temporal evolution of the bubble sizes during the aeration process. We can notice through Fig. 8 that the appearance of bubbles in the liquid bulk starts at time $t/T \approx 4.5$ (see Fig. 8g). Moreover, the flow can be considered as 'bubbly' only at $t/T \approx 5.5$ (Fig. 8k). It is possible to isolate all n bubbles dispersed within the water phase, calculate the volume of each individual bubble $\mathcal{V}_{b,i}$ $(i = 1, n)$, and deduce an approximation of its diameter $d_{b,i} = (6\mathcal{V}_{b,i}/\pi)^{(1/3)}$. Figure 10(a) represents the probability density function of bubble size distribution for $t/T = 10$ using both LES and DNS formulations. Most of the bubble sizes are smaller than the average value d_{bm}. The probability density functions are quasi-similar (see Fig. 10a).

Finally, from an engineering perspective, it is crucial to estimate the air bubble volume dispersed inside the water phase. As mentioned in the introduction, for some applications, bubbles are desirable and for others their presence must be avoided. However, if these air bubbles are produced during a mixing process, it is important to estimate the temporal evolution of the gas holdup, ε:

$$\varepsilon(t) = \mathcal{V}_b/(\mathcal{V}_b + \mathcal{V}_l) \tag{12}$$

which is the ratio of the volume of the air phase entrained within the water, $\mathcal{V}_b = \sum_{i=1}^{n} \mathcal{V}_{b,i}$, to the total volume of air and water within the stirred vessel; $\mathcal{V}_l = \pi D_b^2 h/4$ is the volume of the water phase. In Fig. 10(b), we show the evolution of the gas holdup $\varepsilon(t)$ highlighting its maximum value at $t/T \approx 6.25 - 6.5$ beyond which the dynamic equilibrium amongst bubble formation, coalescence, and breakup leads to a steady ε. Inspection of Fig. 10(b) reveals that the bubbly steady-state using both DNS and LES is reached for $t/T \geq 8$ with about 1.9% of air dispersed in the water bulk. The difference between these approaches is in the interval $t/T \approx 5.5 - 8.0$ where DNS predicts more bubbles compared to LES.

5. Conclusion and perspectives

In this paper, we have studied numerically the complex dynamics occurring during air-liquid mixing using a pitched blade turbine. The motion of the impeller and the fluid-structure interaction is computed by a direct forcing method within a general solver for multiphase flows (Shin et al., 2017). We have shown that vortical structures are similar for any frequency below the aeration limit. These vortical structures correspond to Kelvin-Helmholtz, blade tip, end wall, and wall breakdown vortices. Aeration occurs for a sufficiently large rotational frequency, and we highlight the importance of the initial state (from rest or from an already developed flow). Future research avenues for study are to investigate further the physics of the aeration (for frequency larger than 10 Hz), generalise this study through variation of the initial liquid height, the clearance and the diameter ratio between the impeller and the cylindrical tank. Another type of multiphase mixing process that has not been studied here and occurs for high frequencies $f \geq 15$ Hz, is 'air envelopment' mixing. At very high rotation frequencies, the air phase will envelop the entire impeller during the rotation. It would also be interesting to explore different types of impellers (e.g., Rushton turbines, propellers or curved blade turbines). Finally, in considering non-Newtonian fluids or the presence of surfactants, the recent paper of Shin et al. (2018) has moved the numerical method in those directions and thus these effects could, in the future, be modelled too.

Acknowledgements. DJ and JC acknowledge support through computing time at the Institut du Developpement et des Ressources en Informatique Scientifique (IDRIS) of the Centre National de la Recherche Scientifique (CNRS), coordinated by GENCI (Grand Equipement National de Calcul Intensif) Grant 2021 A0102B06721. LK acknowledges with gratitude P. Dossin, H. Hu and Z. Alam for the warm hospitality at Procter & Gamble where this study has been initiated. O.K.M. also acknowledges funding from PETRONAS and the Royal Academy of Engineering for a Research Chair in Multiphase Fluid Dynamics, and the PETRONAS Centre for Engineering of Multiphase Systems. Simulations have been performed using code BLUE (Shin et al., 2017) and the visualisations have been generated using Paraview.

Funding Statement. This work is supported by the Engineering & Physical Sciences Research Council, United Kingdom, through the MEMPHIS (EP/K003976/1) and PREMIERE (EP/T000414/1) Programme Grants, and by computing time at HPC facilities provided by the Research Computing Service (RCS) of Imperial College London.

Declaration of Interests. The authors declare no conflict of interest.

Author Contributions. All authors have contributed equally to this paper.

Data Availability Statement. Raw data are available from the corresponding author L. K.

Ethical Standards. The research meets all ethical guidelines, including adherence to the legal requirements of the study country.

Supplementary Material. No supplementary materials.

References

Batels, C., Breuer, M., Wechdler, K., & Durst, F. (2020). Computational fluid dynamics applications on parallel-vector computer: computations of stirred vessel flows. *Computer & Fluids 31*, 69–97.

Beckett, C. (2006). *Thatcher.* Haus Publishing, 2006.

Brucato, A., Ciofalo, M., Grisafi, F., & Micale, G. (1998). Numerical prediction of flow fields in baffled stirred vessels: A comparison of alternative modelling approaches. *Chemical Engineering Science 53*(21), 3653–3684.

Ciofalo, M., A. Brucato, A., Grisafi, F., & Torraca, N. (1996). Turbulent flow in closed and free-surface unbaffled tanks stirred by radial impellers. *Chemical Engineering Science 51*(14), 3557–3573.

Daube, O. (1991). Numerical simulation of axisymmetric vortex breakdown in a closed cylinder. *American Math. Soc. 28*, 131–152.

Deardoff J. W. (1970). A numerical study of three-dimensional turbulent channel flow at large Reynolds numbers. *J. Fluid Mech. 41*, 453–480.

Douglas Goff, H. (1997). Colloidal aspects of ice cream - A review. *Int. Dairy J. 7*, 363–373.

Fadlun, E. A., Verzicco, R., Orlandi, P., & Mohd-Yusof, J. (2000). Combined immersed-boundary finite-difference methods for three-dimensional complex flow simulations. *J. Comp. Phys. 161*, 35–60.

Harlow, F. H. & Welch, J. E. (1965). Numerical calculation of time dependent viscous incompressible flow of fluid with free surface. *Phys. Fluids 8*, 2182–2189.

Kwak, D. Y. & Lee, J. S. (2004). Multigrid algorithm for the cell-centred finite difference method ii: Discontinuous coefficient case. *Wiley InterScience (www.interscience. com)*.

Jansson, T. R. N., Haspang, M. P., Jesen, K. .H, Hersen, P., & Bohr, T. (2006). Polygons on a rotating fluid surface. *Phys. Rev. Lett. 96*(4), 174502.

Kahouadji, L. (2011). Linear stability analysis for free surface rotating flow. *PhD thesis*, Université Pierre & Marie Curie - Paris VI.

Kahouadji, L. & Martin Witkowski, L. (2014). Free surface due to a flow driven by a rotating disk inside a cylindrical tank: Axisymmetric configuration. *Phys. Fluids 26*, 072105.

Kahouadji, L., Nowak, E., Kovalchuk, N., Chergui, J., Juric, D., Shin, S., Simmins, M. J. H., Craster, R. V. & Matar, O.K. (2018). Simulation of immiscible liquid-liquid flows in complex micro-channel geometries using a front-tracking scheme. *Microfluidics and Nanofluidics 22*, 126.

Launder, B. E. & Spalding, D. B.(1974). The numerical computation of turbulent flows. *Comp. Meth. Appl. Mech. Engineering 3*, 260–289.

Li, L., Wang, J., Feng, L. & Gu, X. (2017). Computational fluid dynamics simulation of hydrodynamics in an uncovered unbaffled tank agitated by pitched blade turbines. *Korean J. Chem. Eng. 34*(11), 2811–2822.

Lilly, D. K. (1966). On the application of the eddy-viscosity concept in the inertial sub-range of turbulence. *Tech. Rep.* 123. NCAR.

Lilly, D. K. (1966). The representation of small-scale turbulence in numerical simulation experiments. *Proc. IBM Scientific Computing Symposium on Environmental Sciences.* IBM Data Processing Division, White Plains, New York.

Lopez, J. M. (1995). Unsteady swirling flow in an enclosed cylinder with reflectional symmetry. Phys. Fluids *7*, 2700–2714.

McClements, D. J. (2004). *Food Emulsions: Principles, Practices, and Techniques* 2nd Edition. CRC Press.

Mc Millan, O. J. & Ferziger, J. H. (1979). Direct testing of subgrid-scale models. *AIAA J. 17*, 1340?1346.

Meyers, J. & Sagaut, P. (2006). On the model coefficients for the standard and the variational multi-scale Smagorinsky model. *J. Fluid Mech. 569*, 287–319.

Mohd-Yusof, J. (1997). Combined immersed-boundary / b-spline methods for simulations of flow in complex geometries. *Center for Turbulence Research Annual Research Briefs* 317–327.

Peskin, C. S. (1977). Numerical analysis of blood flow in the heart. *J. Comp. Phys. 25*, 220–252.

Piva, M. & Meiburg, E. (2005). Steady axisymmetric flow in an open cylindrical container with a partially rotating bottom wall. *Phys. Fluids 17*, 063603.

Poncet, S. (2005). Écoulements de type rotor-stator soumis à un flux axial: de batchelor à stewartson. *PhD thesis*, Université de Provence Aix-Marseille I.

Pope, S. B. (2000). *Turbulent Flows.* Cambridge: Cambridge University Press.

Pope, S. B. (2004). *Ten questions concerning the large-eddy simulation of turbulent flows. New Journal of Physics 6*, 35.

Saad, Y. (2003). Iterative Methods for Sparse Linear Systems. *Society for Industrial and Applied Mathematics*, 2nd Edition.

Shin, S. (2007). Computation of the curvature field in numerical simulation of multiphase flow. *J. Comp. Phys. 222*, 872–878.

Shin, S., Chergui, J. & Juric, D. (2017). A solver for massively parallel direct numerical simulation of three-dimensional multiphase flows. *J. Mech. Sci. Tech. 31*, 1739.

Shin, S., Chergui, J., Juric, D., Kahouadji, L., Matar, O.K. & Craster, R. V. (2018). A hybrid interface tracking-level set technique for multiphase flow with soluble surfactant. *J. Comp. Phys. 359*, 409–435.

Shin, S. & Juric, D (2009). A hybrid interface method for three-dimensional multiphase flows based on front tracking and level set techniques. *Int. J. Num. Meth. Fluids 60*, 753–778.

Smagorinsky, J. (1963). General Circulation Experiments with the Primitive Equations. I. The Basic Experiment. *Month. Wea. Rev. 91*, 99–164.

Spohn, A. (1991). Écoulement et éclatement tourbillonnaire engendré par un disque tournant dans une enceinte cylindrique. *PhD thesis*, Université de Grenoble I.

Spohn, A., Mory, M., & Hopfinger, E. (1993). Observations of vortex breakdown in an open cylindrical container with a rotating bottom. *Exp. Fluids 14*, 70–77.

Spohn, A., Mory, M., & Hopfinger, E. (1998). Experiments on vortex breakdown in a confined flow generated by a rotating disc. *J. Fluid Mech. 370*, 73–99.

Stewartson, K. (1953). On the flow between two rotating coaxial disks. *Proc. Camb. Phil. Soc. 49*(9) 333–341.

Suzuki, T., Iima, M., & Hayase, Y. (2006). Surface switching of rotating fluid in a cylinder. *Phys. Fluids 18*, 101701.

Vatistas, G. H. (1990). A note on liquid vortex sloshing and Kelvin's equilibria. *J. Fluid Mech. 217*, 241–248.

Vatistas, G. H., Wang, J., & Lin, S. (1992). Experiments on waves induced in the hollow core vortices. *Exp. Fluids 13*, 377–385.

Witz, C., Treffer, D., Hardiman, T., & Khinast, J. (2016). Local gas holdup simulation and validation of industrial-scale aerated bioreactors. *Chem. Eng. Sci. 152*, 636–648.

Cite this article: Kahouadji, L., Liang, F., Valdes, J. P., Shin, S., Chergui, J., Juric, D., Craster, R. V., & Matar, O. K. (2022). The transition to aeration in turbulent two-phase mixing in stirred vessels. *Flow*, *x*, 1–18. doi:xxx